Materials Science & Engineering A 709 (2018) 193–202

Contents lists available at ScienceDirect

Materials Science & Engineering A

journal homepage: www.elsevier.com/locate/msea

# Influence of 3D connectivity of rigid phases on damage evolution during tensile deformation of an AlSi12Cu4Ni2 piston alloy

Katrin Bugelnig[a,*], Federico Sket[b], Holger Germann[c], Thomas Steffens[c], Robert Koos[d], Fabian Wilde[e], Elodie Boller[f], Guillermo Requena[g,h]

[a] Institute of Materials Science and Technology, Technical University of Vienna, Karlsplatz 13/E308, A-1040 Vienna, Austria
[b] IMDEA Materials Institute, C/ Eric Kandel 2, 28906 Getafe, Spain
[c] KS Kolbenschmidt GmbH, Karl-Schmidt-Straße, 74172 Neckarsulm, Germany
[d] FRM II, TU München, Lichtenbergstraße 1, 85748 Garching, Germany
[e] Helmholtz-Zentrum Geesthacht, Zentrum für Material, und Küstenforschung GmbH, Max-Planck-Straße 1, 21502 Geesthacht, Germany
[f] ESRF-The European Synchrotron, CS40220 Grenoble Cedex 9, France
[g] German Aerospace Centre, Linder Höhe, 51147 Cologne, Germany
[h] Metallic Structures and Materials Systems for Aerospace Engineering, RWTH Aachen University, Aachen 52062, Germany

ARTICLE INFO

*Keywords:*
Characterization
Fracture behaviour
Stress/strain measurements
Aluminium alloys
Intermetallics
Synchrotron tomography

ABSTRACT

The microstructural evolution during solution treatment at 500 °C of a cast AlSi12Cu4Ni2 piston alloy is evaluated by two dimensional and three dimensional imaging methods aiming at identifying the microstructural features affecting the processes of damage formation and accumulation under tensile deformation. Highly interconnected networks of aluminides and Si undergo a local loss of connecting branches within these networks owing to the partial dissolution of Cu-rich aluminides and a slight Si spheroidisation. The damage by tensile deformation is studied using synchrotron tomography during in situ tensile tests. In both studied heat treatment conditions (0 h and 4 h solution treated) damage initiates in the form of micro-cracks in clusters of primary Si particles and debonding at the interface between Si and the matrix. These micro-cracks grow through intermetallic phases in the last stages of deformation. Final failure occurs by coalescence of these cracks mainly through the rigid phases. The loss of connectedness of the Si-intermetallics network during solution treatment allows the alloy to accommodate more damage and plastic strain resulting in an increase of ductility with respect to the as cast condition.

## 1. Introduction

Near eutectic Al-Si alloys show excellent castability, good wear resistance and low thermal expansion, which makes them a favourable choice for pistons in high performance combustion engines [1]. Pistons are a vital part of the engine and happen to be one of the most thermo-mechanically stressed parts of the entire vehicle. Thus, they are a continuous subject of further development for optimization and adaption to new engines with ever higher efficiencies. [2].

The microstructure of cast near eutectic Al-Si piston alloys consists of interconnected 3D hybrid networks formed by Si (primary and eutectic) and intermetallic phases embedded in a comparatively soft α-Al matrix [3–8]. The load carrying capability of these networks is affected by topological and morphological changes that they can undergo during thermal heat treatments and due to the thermo-mechanical conditions during service [4,5,9–11]. Thus, thermal treatments of near eutectic Al-Si piston alloys at temperatures close to 500 °C typically result in the (partial) dissolution of intermetallic phases such as $Mg_2Si$ and $Al_2Cu$ as well as in the spheroidisation (fragmentation, coarsening and rounding) of eutectic Si [3,10,11]. As a consequence, the interconnectivity of the 3D networks of rigid phases decreases and the mechanical performance of the alloys is affected [3–5,12,13]. It has been shown that the addition of about 1–2 wt% Ni to a binary AlSi12 alloy has a retarding effect on the disintegration of the Si network [3,12]. Contrarily to AlSi12, the AlSi12Ni alloy remains highly interconnected after solution treatment owing to high contiguity between aluminides and Si. The addition of aluminide-forming elements such as Ni, Cu and Mg leads to a thermally more stable rigid phase network, which, consequently, allows the alloys to retain their strength at elevated temperatures compared to binary Al-Si near eutectic alloys [3,12,14]. The 3D networks in near eutectic Al-Si alloys with additions of Cu, Ni and Mg remain highly interconnected even after 4 h of solution treatment at 500 °C [13]. Thus, the presence

* Corresponding author. Present address: German Aerospace Centre, Linder Höhe, 51147 Cologne, Germany.
*E-mail addresses:* katrin.bugelnig@tuwien.ac.at, Katrin.Bugelnig@dlr.de (K. Bugelnig), guillermo.requena@dlr.de (G. Requena).

http://dx.doi.org/10.1016/j.msea.2017.10.035
Received 8 August 2017; Received in revised form 10 October 2017; Accepted 12 October 2017
Available online 14 October 2017

**Table 1**
Experimental parameters for the tomography experiments.

| Beamline: | Experiment: | Energy: [keV] | voxel- size: [$\mu m^3$] | Sample-to- detector distance: [mm] | Exposure time: [msec/ proj] | Nr. of Proj.: | total scan time: [h] |
|---|---|---|---|---|---|---|---|
| **ID19/ESRF** | **Solution Heat Treatment (ST)** (0 h/500 °C vs. 4 h/500 °C) | 19 | $(0.3)^3$ | ~ 3 and 16 | 300 | 2000 | 0.2 |
| **P05/Petra III** | **Interrupted in-situ RT tensile tests** (0 h/500 °C vs. 4 h/500 °C) | 25 | $(1.2)^3$ | 30 | 1100 | 900 | 1.5 |

of about 20 vol% of highly interconnected networks formed by eutectic Si and Ni-, Cu-, and/or Fe-rich aluminides leads to higher room temperature (RT) and elevated temperature strength after solution treatments while the binary AlSi12 alloy completely loses the interconnectivity of eutectic Si [15].

The process of damage accumulation during tensile deformation for this type of alloys is characterized by the formation of micro-cracks in the stiffer phases that can lead to coalescence among micro-cracks and failure during further loading [3,6]. Microcracks were observed to be formed perpendicularly to the loading axis in regions were Cu-, Ni- and Fe-rich aluminides and eutectic Si display short-fibre-like morphologies and are oriented ± 30 ° with respect to the load direction [3]. Furthermore, larger volume fractions of rigid phases may result in damage onset at earlier stages during deformation [16,17]. Also, it has been found that the evolution of damage in an AlSi12Ni alloy is strongly related to the geometry of the intermetallic phases present in the material [18]. It was observed that small clustered aluminide structures are prone to break off at an earlier stage of tensile deformation than larger ones.

In contrary to ductile damage, which can normally be observed as a massive bulk phenomenon, damage in Al-Si piston alloys occurs in a localized manner and, as such, 2D investigations are insufficient to unequivocally identify the microstructural features that lead to crack initiation and damage accumulation (low number density of cracks). A possible way to overcome this issue is by in-situ synchrotron X-ray computed tomography (sXCT) during deformation [19–23]. This technique is better suited than laboratory X-ray tomography since much faster acquisition times can be achieved and the phase contrast provided by some synchrotron imaging beamlines [24,25] can be used to reveal phases with similar attenuation such as the eutectic and primary Si embedded in the α-Al matrix [5].

The aim of this study is to identify and quantify the changes in the 3D microstructure of a cast AlSi12Cu4Ni2 piston alloy during solution treatment (ST) and the correlation of these changes with the mechanisms of damage formation and the process of damage accumulation during tensile deformation. Conventional metallography and synchrotron tomography are combined to analyse microstructural evolution, while in situ synchrotron tomography during tensile deformation is used to study the damage evolution.

## 2. Experimental

### 2.1. Materials

The investigated material is a near eutectic Al-Si piston alloy with 12 wt% Si, 4 wt% Cu and 2 wt% Ni (AlSi12Cu4Ni2). Piston raw parts produced by gravity die casting were provided by Kolbenschmidt GmbH. All samples were taken from the bowl rim area of these diesel pistons. The alloy was studied in two different conditions: in the first condition, the material was not subjected to solution heat treatment (0 h ST). In the second condition the alloy was solution treated for 4 h at 500 °C followed by water quenching (termed 4 h ST). The alloy in both ST conditions was then aged for 5 h at 230 °C and subsequently overaged for 100 h at 300 °C to stabilize the precipitation condition (air cooled after each ageing step).

### 2.2. Methods

Light optical microscopy (LOM) and scanning electron microscopy (SEM) were complemented by synchrotron X-ray computed tomography (sXCT). The use of sXCT instead of conventional x-ray tomography (XCT) was necessary because of the very similar X-ray attenuations of α-Al and Si that can only be revealed separately by phase contrast [14].

Micro-hardness of the alloy in both conditions was evaluated by Brinell-hardness HB (1/10) tests. Furthermore, Nano-hardness tests of the α-Al matrix in both ST + ageing conditions were carried out using a *UMIS Nanoindentation System 2K0A*. For this, an indenter of the type Berkovich was applied load-controlled with a maximum load of 3mN and a loading rate of 0.15mN/s. After a dwelling time of 30 s it was unloaded with 0.3 mN/s. In order to obtain statistically relevant values, indentations were carried out in at least 30 positions (3 groups with 10 indentations each) for each alloy condition.

#### 2.2.1. Influence of solution heat treatment on the 3D microstructure

The evolution of the 3D microstructure was studied for the same sample in the 0 h ST condition and after 4 h ST by sXCT at the beamline ID19 of the European Synchrotron Radiation Facility (ESRF) in Grenoble, France. For this, cylindrical specimens with diameters of 0.6 mm were machined. Table 1 displays the experimental conditions. The sXCT scans (voxel size = $(0.3\ \mu m)^3$) were carried out using two distances between sample and detector: a small distance of 3 mm was used to avoid phase contrast effects at the interface of aluminides and, thus, obtain a reliable segmentation of these intermetallic phases, while a distance of 16 mm was used to reveal eutectic and primary Si in the α-Al matrix.

The identification of intermetallic phases in both conditions was carried out by SEM and electron dispersive spectroscopy (EDS).

#### 2.2.2. Influence of solution heat treatment on the damage behaviour of the alloy

Interrupted in-situ tensile tests were conducted at RT at the micro tomography end station of beamline P05 of synchrotron source PETRA III at DESY in Hamburg, Germany [25]. Flat tensile samples with 1 $mm^2$ cross-section and a parallel gauge length of 2 mm were produced by spark erosion. An in-situ tensile rig provided by IMDEA Materials, Spain, was positioned on the rotating table. Figures of the sample geometry and the experimental setup used for these experiments can be found elsewhere [7]. Table 1 shows the parameters for the sXCT scans (voxel size = $(1.2\ \mu m)^3$) acquired during the interrupted in-situ tensile tests. The first tomography was acquired before deformation and several tomographies were then subsequently acquired after applying increasing deformation steps until fracture. The load steps for scans were chosen to be mainly in the plastic deformation range rather than in the elastic range of the material and were determined with ex-situ tensile tests with the same tensile rig and sample geometry prior to the in-situ experiments.

The imaged volume was kept at the centre of the specimen to be

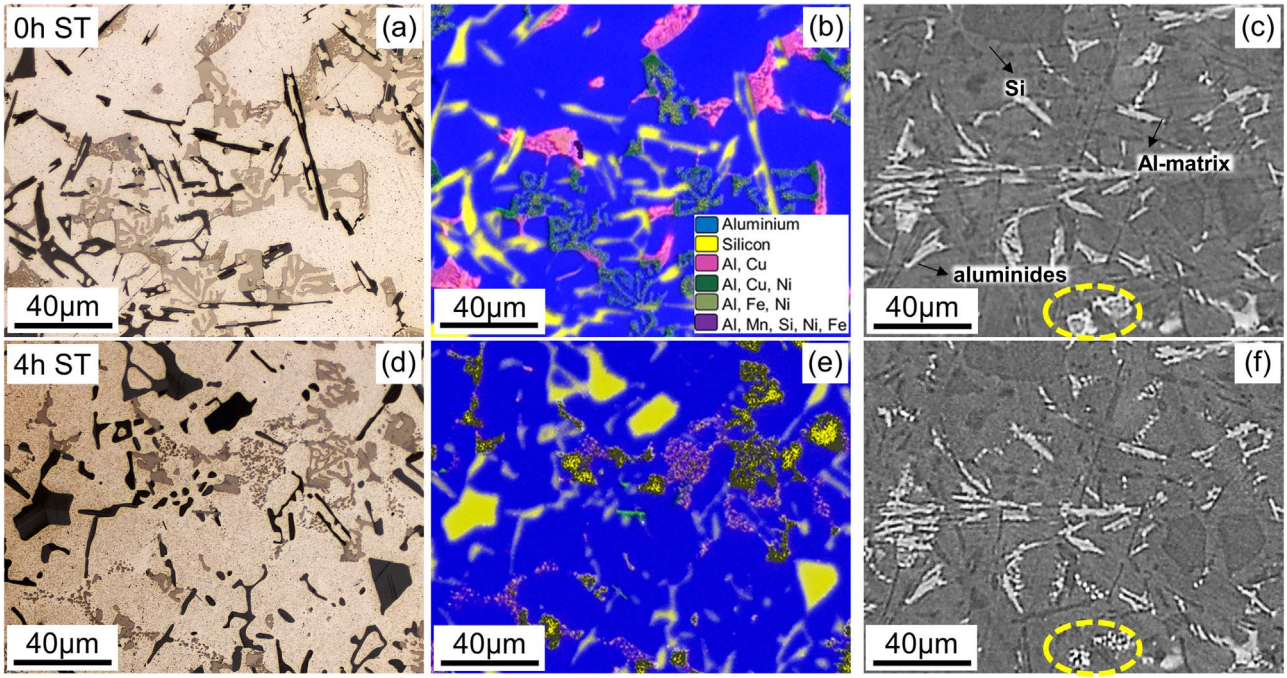


**Fig. 1.** 2D microstructure of the AlSi12Cu4Ni2 alloy (a-c) 0 h ST condition: (a) LOM showing primary and eutectic/primary Si (dark) and intermetallic phases (bright) embedded in the α-Al matrix, (b) SEM/EDS mapping with the elements identified indicated, (c) Portion of a reconstructed synchrotron tomography slice (ID19-ESRF, voxel size = (0.3 µm)$^3$); (d-f) 4 h ST condition: (d) LOM, (e) SEM/EDS mapping, (f) synchrotron tomography slice of the same region as in (c).

able to follow the damage evolution in this region. The deformation rate was 2 µm/s. The test was stopped and the displacement was kept constant during the tomographic scan to avoid artefacts.

The reconstructed tomographies were used to determine the global strain in the investigated volume at each loading condition: the distance between aluminide particles at the top and particles at the bottom of the imaged volume was measured at each load step. The strain, $\varepsilon$, was then calculated considering the change in distance $\Delta l$ between the particles with increasing load, $\varepsilon = \Delta l/l_0$, where $l_0$ is the initial distance between the pair of particles at the beginning of the tensile test. The mean strain, ε and the standard deviation of the distances between at least ten pairs of particles were computed to obtain statistically relevant values.

### 2.2.3. Image analysis

*2.2.3.1. Pre-processing.* The reconstructed 32 bit tomographic slices were assembled to stacks and converted to 8 bit using the software Fiji [26]. Rigid registration of the volumes obtained for the samples before and after solution treatment was carried out using Avizo Fire 8.1.

For the tensile tests non-linear and affine registrations were conducted to register the volumes at different loading steps using the softwares MedInria [27] and Fiji, respectively.

*2.2.3.2. Image segmentation.* Prior to segmentation, the reconstructed volumes were filtered using a 3D median filter (radius = 1 pixel) and a 2D anisotropic diffusion filter (5–10 iterations) available in Fiji. The tomographies acquired with the lowest sample-to-detector distance (~ 3 mm - see Table 1) were used for the segmentation of aluminides owing to the minimum phase contrast effects at their borders. On the other hand, tomographies obtained with a sample to detector distance of 16 mm were used for the segmentation of Si particles revealed by phase contrast. However, the higher phase contrast at this sample-to-detector distance results in artefacts at the interface between aluminides and the α-Al matrix that can easily be mistaken as eutectic Si. To minimize segmentation errors from this effect, the aluminides segmented in the tomographies at 3 mm sample-to-detector distance were overlapped to the tomographies at 16 mm after being dilated by 1 pixel. This procedure allows to get rid of the phase contrast artefacts at the aluminide/matrix-interfaces to a large extent and hence, to achieve a more accurate evaluation of Si particles. Nonetheless, an automatic segmentation of Si particles over a large volume was still not possible by simple global grey value threshold. Therefore, manual segmentation of Si particles was carried out using the imaging software Avizo Fire 8.1.

Segmentation of aluminides was carried out using three different global threshold values (ideal threshold determined by eye ± 2 grey values) to increase the representativeness of quantitative analyses. 3D visualizations of regions of interest were produced using the softwares Avizo Fire 8.1 and VG Studio Max 2.2.

*2.2.3.3. Characterization of the 3D microstructure and damage.* For the characterization of the evolution of the 3D microstructure with solution treatment (ESRF/ID19), the quantitative parameters volume fraction $V_f$, interconnectivity, $I$, and Euler number were calculated for the aluminides.

The interconnectivity of aluminides is computed as the volume of the largest particle divided by the total volume of aluminides [3,8]. The Euler number is a topological parameter which allows conclusions about the changes in local connectivity or *connectedness* in complex 3D networks. While the global interconnectivity of a large 3D network might remain constant, variations in the Euler number indicate local connectivity changes such as loss or formation of connecting branches within a 3D network [28,29]. The Euler number is defined as:

$$\chi = N + N_{Cavities} - N_{Tunnels} \quad (1)$$

Where N indicates the number of particles, $N_{Cavities}$ the number of cavities and $N_{Tunnels}$ the number of tunnels within a network [30]. The lower the Euler number, the higher the connectedness of the 3D network. An increase in the Euler number means a loss of connecting branches within the network.

## 3. Results

Fig. 1(a) shows the 2D microstructure of the investigated alloy in

**Table 2**
Brinell-hardness of the alloy and nano-hardness of the α-Al matrix in 0 h and in 4 h solution heat treated (ST) condition.

| Condition: | HB (1/10) | H [GPa] |
|---|---|---|
| **0** h/500 °C + 5 h/230 °C + 100 h/300 °C | 85 ± 2.31 | 1.06 ± 0.057 |
| **4** h/500 °C + 5 h/230 °C + 100 h/300 °C | 71 ± 0.55 | 1.09 ± 0.029 |

0 h ST condition acquired by LOM. The microstructure consists of bulky primary and plate-like eutectic Si (darkest phases), and aluminides (bright phases) embedded in the α-Al matrix. SEM/EDS mappings reveal the presence of several intermetallic phases (see Fig. 1(b)) with the following combination of elements: Al-Cu (most probably $Al_2Cu$ [3,10,31,32]), Al-Cu-Ni, Al-Fe-Ni, Al-Mn-Fe-Ni-Si phases. Although the same elements as in the 0 h ST condition were identified in the intermetallic phases, some differences can be observed. First, the original irregular $Al_2Cu$ particles transform into sponge-like structures after 4 h of solution treatment. Moreover, a typical spheroidisation effect is observed for the eutectic and primary Si, resulting in more rounded morphologies and less sharp corners after solution treatment [9,11,13,33].

Fig. 1(c,f) display portions of reconstructed tomographic slices of the microstructure in the same position of a sample scanned at 0 h ST and after 4 h ST. The bright regions correspond to aluminides, while bulky primary and plate-like eutectic Si particles are seen in dark grey. The previously mentioned evolution of the $Al_2Cu$ phase into sponge-like structures is highlighted by the dashed ellipsoids.

Table 2 presents the results of the Brinell-hardness of the alloy and nano-hardness of the α-Al matrix. The nano-hardness remains constant after 4 h ST revealing that the precipitation state is comparable for both studied conditions. However, a drop of about 15% is observed for the Brinell-hardness of the alloy in the 4 h ST condition.

### *3.1. 3D analysis of the influence of solution heat treatment on the microstructure*

Fig. 2a) and b) show details of reconstructed tomographic slices of the microstructure at 0 h ST and after 4 h ST, respectively. The morphological evolution of $Al_2Cu$ mentioned above can be clearly observed in the 2D slices, while the 3D inserts indicate that a partial dissolution of these particles takes place during solution treatment. On the other hand, the Fe- and Ni-containing aluminides did not show any significant morphological changes during ST. Additionally, slight coarsening and spheroidisation of Si particles (dark grey particles) is visible in Fig. 2(c-d) (indicated by yellow circles and in their corresponding 3D views on the right of the figures). Fig. 3 presents an overlay of a portion of an $Al_2Cu$ particle at 0 h ST (blue) and after 4 h ST (red) showing that partial dissolution results in a loss of local connectivity (loss of connectedness) within the aluminides network during ST (see circled areas). While the displayed network shows a global interconnectivity (*I*) of 99.8% and an Euler number of −38 in the 0 h condition, *I* slightly decrases by about 1% (to 98.85%) while the Euler number increases by about 11 (to −27).

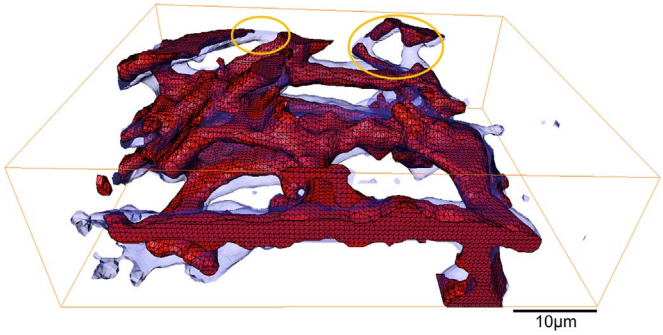


**Fig. 3.** Dissolution and loss of local connectivity of aluminides: overlay of aluminides networks in 0 h ST condition (blue) (global interconnectivity I) = 99.8%, Euler number = −38) and after 4 h ST (red) (I = 98.85%, Euler number = −27). Volume size = 22 × 35 × 10µm$^3$, vox. size = (0.3 µm)$^3$. (For interpretation of the references to color in this figure legend, the reader is referred to the web version of this article.)

Fig. 4 shows 3D visualizations of aluminides in a volume of 230 × 230 × 540 µm$^3$ for the same region of one and the same sample at 0 h ST and after 4 h ST. Different colours have been assigned to each individual particle within the investigated volume. These results reveal a highly interconnected 3D network of aluminides (blue particle) as it has

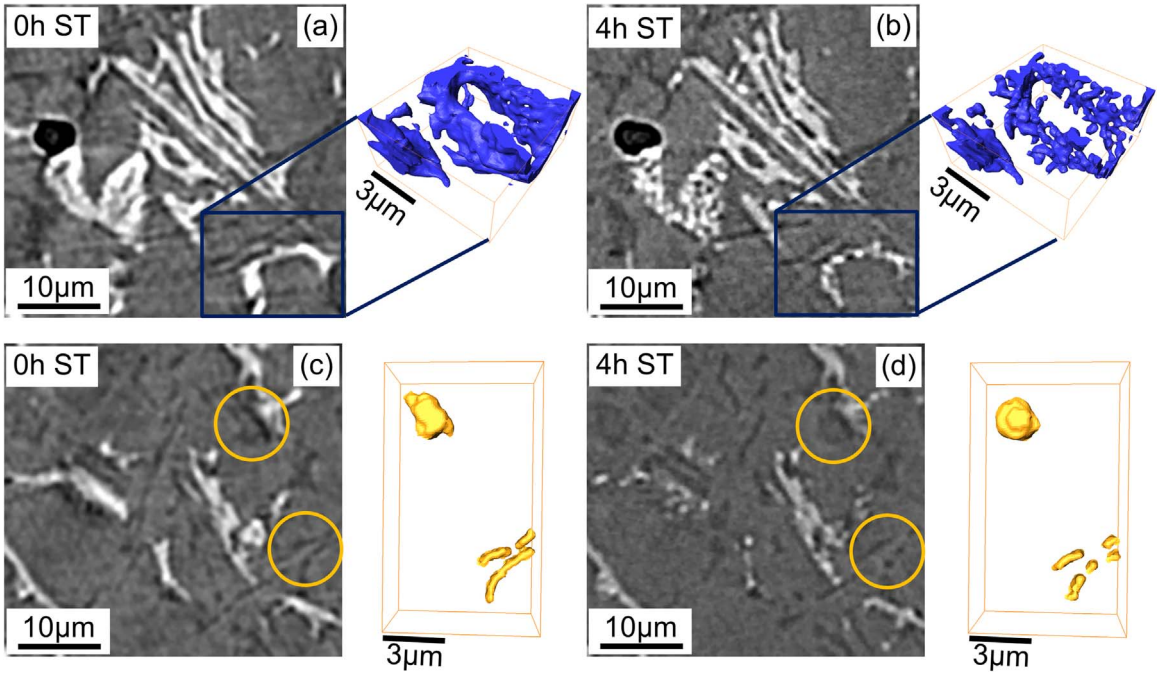


**Fig. 2.** Partial dissolution and morphological changes of Cu-rich aluminides: (a) 0 h ST condition, (b) same region after 4 h ST condition. Spheroidization of Si: (c) 0 h ST condition, (d) same region after 4 h ST condition where changes in primary and eutectic Si are indicated by circles.

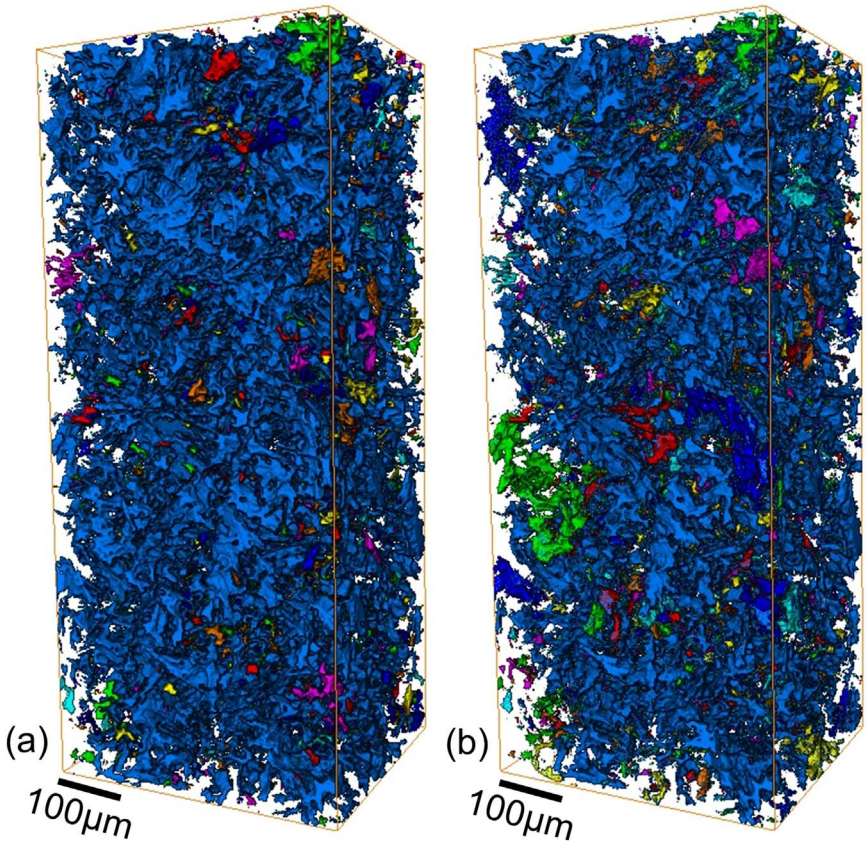


**Fig. 4.** Rendered volumes of the network of aluminides: (a) 0 h ST and (b) same region after 4 h ST. Volume size = 230 × 230 × 540µm$^3$, vox. size = (0.3 µm)$^3$. Each color corresponds to an individual particle with the investigated volume. (For interpretation of the references to color in this figure legend, the reader is referred to the web version of this article.)

been observed for similar Al-Si piston alloys [3]. A partial fragmentation of the aluminides network and, consequently, an increase in the number of non-connected particles within the investigated volume can be observed after 4 h ST (Fig. 4(b)). A quantitative evaluation is commented in the discussion.

### 3.1.1. *Influence of solution treatment on damage accumulation*

Fig. 5(a) shows the stress-strain curves acquired during the interrupted in-situ tensile tests. The strain, $\varepsilon$, corresponds to the mean strain obtained according to the procedure described in chapter 2.2, while the error bars indicate the standard deviation of this calculation. The star-like symbols in Fig. 5 indicate the conditions at which sXCT was conducted. The 0 h ST condition shows about 8% higher strength and lower strain to failure behaviour than 4 h ST. On the other hand, the solution treated condition shows a less stiff behaviour and considerable strain hardening that extends up to failure of the sample. Fracture occurred at ~ 215 MPa and a strain of 1.6 ± 0.6% for 0 h ST, while the alloy after 4 h ST failed at ~ 200 MPa at an elongation at fracture of 3.6 ± 1.4%.

Fig. 6(a–b) shows the damage accumulation (red) during the last three loading steps before failure as well as in the post-mortem condition. The process of damage is characterized by the formation of small cracks heterogeneously distributed along the gauge length. Furthermore, a larger number and volume fraction of cracks can be observed after solution treatment indicating that this condition is able to accommodate more damage before final failure of the alloy than the 0 h ST condition. Damage can be observed first - at the applied spatial

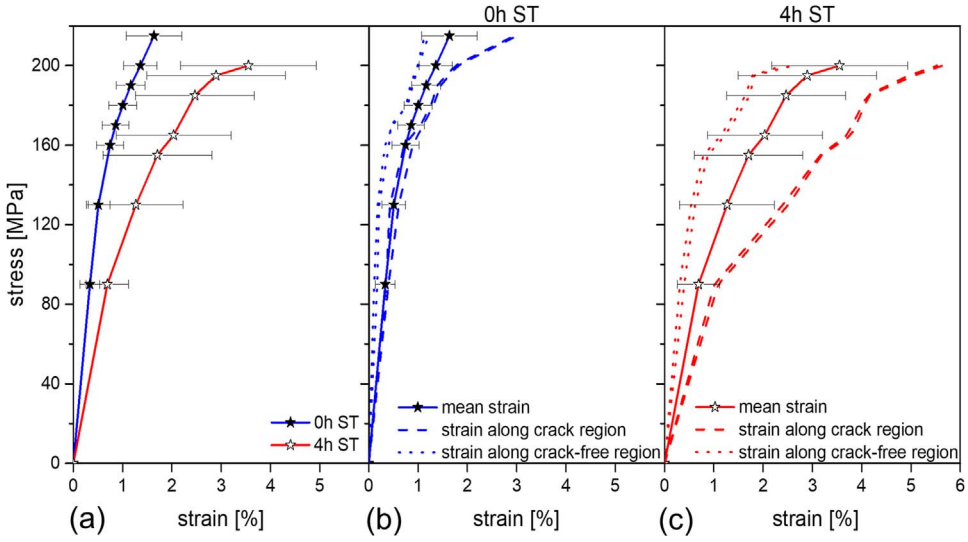


**Fig. 5.** (a) mean stress-strain curves obtained during the interrupted in-situ tensile tests for 0 h ST (blue) and 4 h ST (red) conditions; calculated strain along two regions with cracks (dashed) and along two crack-free regions (dots) for (b) 0 h ST and (c) 4 h ST conditions. The star-like symbols indicate the conditions at which synchrotron tomography was conducted. (For interpretation of the references to color in this figure legend, the reader is referred to the web version of this article.)

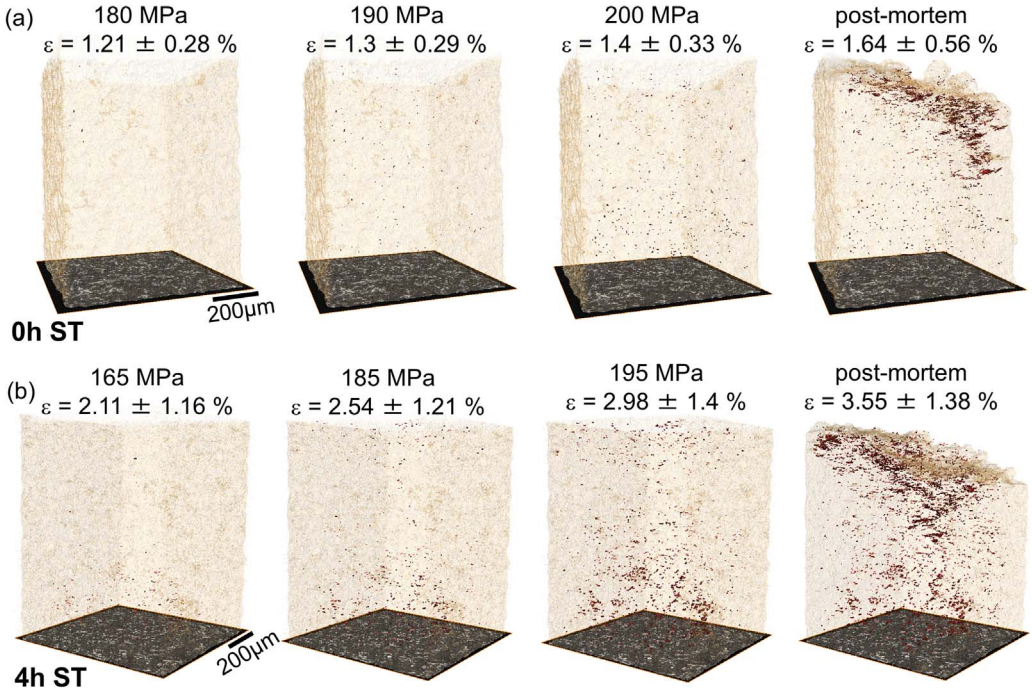


**Fig. 6.** 3D visualization of damage accumulation (red) near the fracture surface during the interrupted tensile tests: a) 0 h ST and b) after 4 h ST. The load direction is vertical. (For interpretation of the references to color in this figure legend, the reader is referred to the web version of this article.)

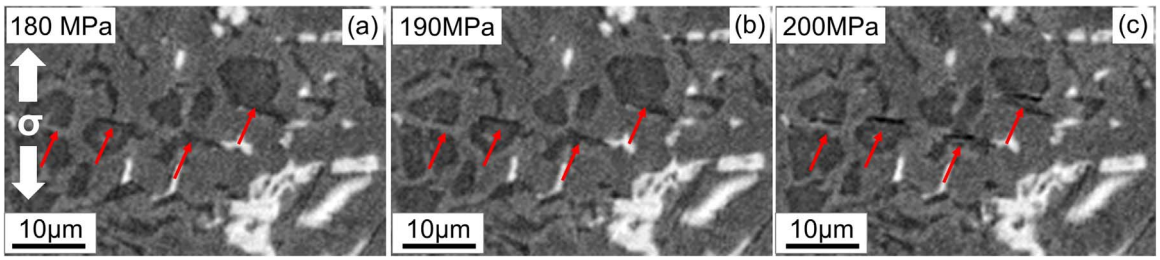


**Fig. 7.** Microcracks through primary Si particles and debonding at matrix-Si interface at several load steps of the alloy in 0 h ST condition. The load direction is vertical.

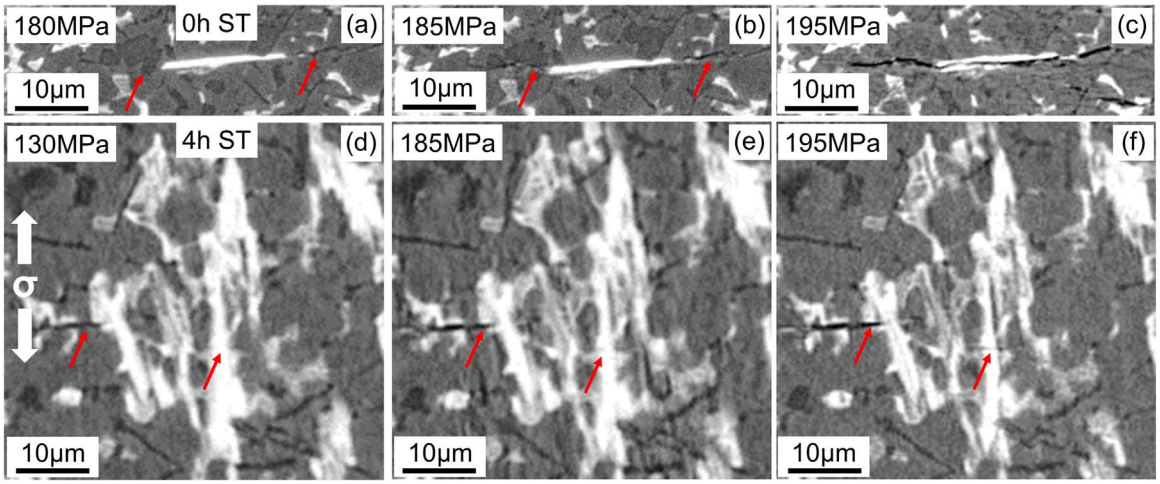


**Fig. 8.** Fracture of Si particles and aluminides at several load steps of the alloy in (a–c) 4 h ST and (d–f) 0 h ST. The load direction is vertical.

resolution - at σ ~ 170 MPa for the 0 h ST condition. On the other hand, damage was detected already at σ ~ 90 MPa for the 4 h ST condition. It must be pointed out that although there is a significant difference in stress at damage initiation between both conditions, the mean strain is similar, i.e. ε ~ 0.85 ± 0.28% and ε ~ 0.7 ± 0.4% for 0 h ST and 4 h ST, respectively. A calculation of the strain along regions where cracks formed and along crack-free regions is shown in Fig. 5(b–c) for the 0 h ST and 4 h ST conditions, respectively. These strains where calculated along two regions with cracks as well as along two regions without cracks. It can be clearly observed that the strains in regions where damage forms and accumulates are much higher than the strains in crack-free regions indicating that damage initiation is strain-driven. Representative images of the dominant damage mechanisms are presented in the 2D slices in Fig. 7 and Fig. 8 for the 0 h and 4 h ST conditions, respectively. Damage initiates in both conditions predominantly as a mixture of micro-cracks through primary Si particles

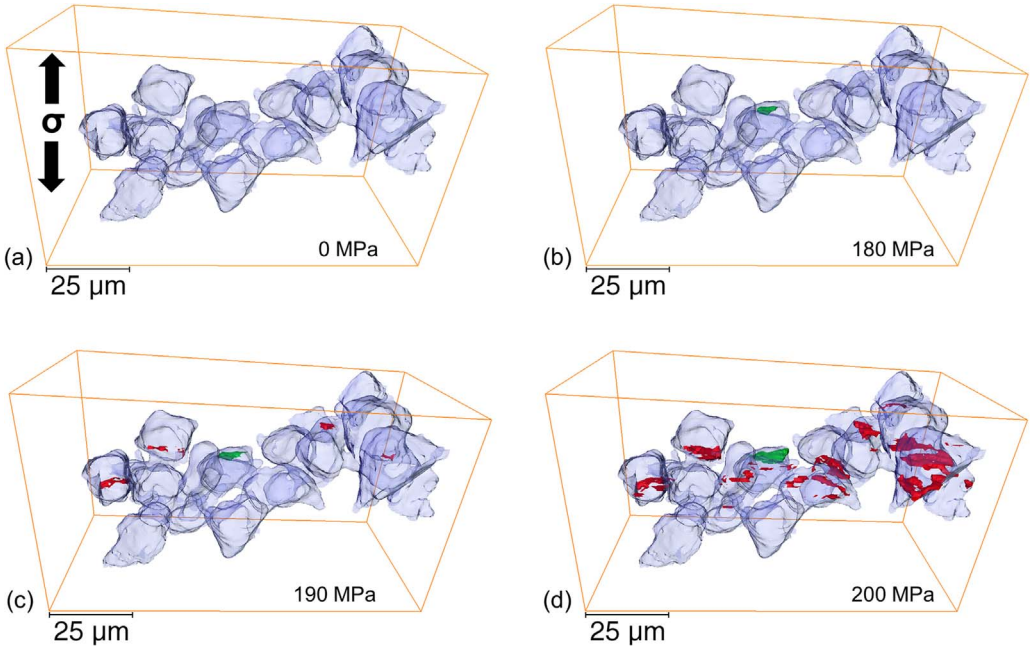


**Fig. 9.** 3D visualization of damage accumulation in a cluster of primary Si particles (blue) for the alloy in 0 h ST condition: a) undamaged Si particles at 0 MPa, (b) debonding (green) at Al-Si interface (applied stress = 180 MPa), c) microcracks formation (red) (applied stress = 190 MPa), d) further formation and growth of microcracks at an applied stress of 200 MPa. The α-Al matrix and the intermetallic phases are transparent. (For interpretation of the references to color in this figure legend, the reader is referred to the web version of this article.)

and debonding between Si (predominantly primary Si) and matrix (Fig. 7). The micro-cracks tend to form perpendicularly to the load direction. In general, formation of cracks at aluminides occurs in the final stages of deformation, usually as micro-cracks formed at primary Si particles that propagate through adjacent aluminide particles (Fig. 8).

Fig. 9 and Fig. 10 show 3D visualizations of the 2D regions presented in Fig. 7 and Fig. 8 for the 0 h and 4 h ST conditions, respectively. Besides the formation of micro-cracks (red) in primary Si particles (blue) and debonding at the Si-matrix interface (green) it can be observed that damage accumulates in an area where primary Si particles form clusters or chain-like arrangements (see Fig. 7 and Fig. 9). Cracks through aluminides only occurred at a late stage of the tensile test mainly by propagation of cracks formed at neighbouring Si particles (see Fig. 8 and Fig. 10). Randomly distributed processing pores accounting a total volume fraction of ~ 0.1 vol% (see for example Fig. 2(a)) could be observed in the investigated alloy. Damage was not detected initiating from this processing porosity in any of the studied conditions.

The correlation between the damage mechanisms previously described and the evolution of the main crack leading to failure of the alloys can be observed qualitatively in Fig. 11. Representative portions of 2D slices of the 0 h and 4 h ST conditions at loads where damage can be observed, particularly at Si particles, are presented in Fig. 11a) and c), respectively. The same regions after fracture of the samples are shown in Fig. 11b) and d). It can be seen that the main crack propagates along the rigid phases passing through pre-existing micro-cracks in both conditions. Fig. 11(e-f) presents the fracture surfaces (blue) of the 0 h ST and 4 h ST conditions, respectively. Micro-cracks existing along the main crack path at the last load step before failure are indicated in red. While the 0 h ST condition only shows a few pre-existing micro-cracks, the 4 h ST condition presents a significantly higher accumulation of pre-existing cracks along the fracture surface. Cracks through primary Si particles located on the fracture surface are shown in green in the detailed insert in Fig. 11(f).

## 4. Discussion

Solution treatment of the AlSi12Cu4Ni2 alloy at 500 °C during 4 h results in the partial dissolution and, consequently, morphological evolution of the Al2Cu phase from irregular blocky particles to sponge-like structures, while the morphology of Fe- and Ni-rich aluminides

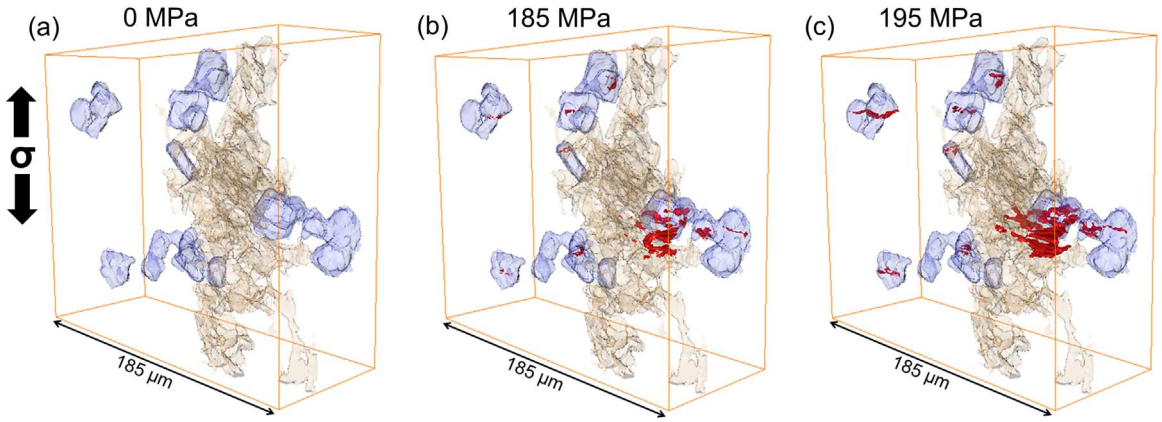


**Fig. 10.** 3D visualization of damage accumulation in a region with a cluster of Si particles (blue) partially connected to an aluminide particle (brown) in the alloy after 4 h ST: (a) initial condition at 0 MPa, (b) formation of microcracks at Si particles at an applied stress of 185 MPa, (c) growth of microcracks and propagation into an adjacent aluminide particle at 195 MPa. The Al-matrix is transparent. (For interpretation of the references to color in this figure legend, the reader is referred to the web version of this article.)

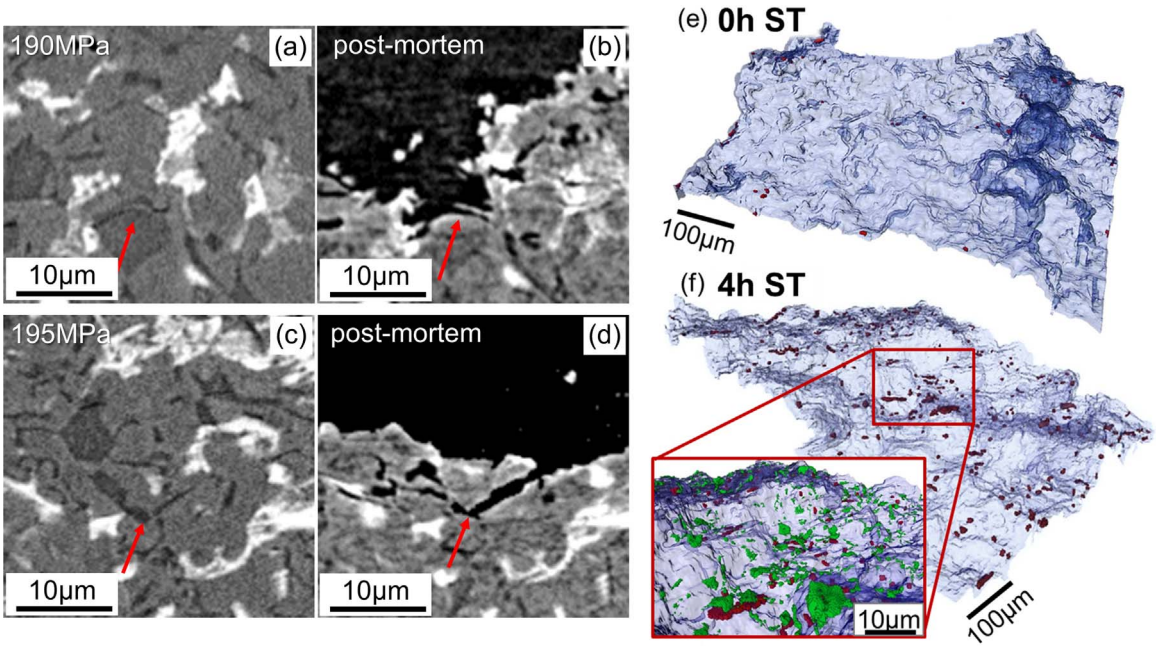


**Fig. 11.** Main crack propagates along rigid phases and pre-existing micro-cracks: (a, b) 0 h ST (c, d) 4 h ST. 3D fracture surface with cracks (red) mainly through primary Si (green) at last load step before failure (e) at 0 h ST, (f) after 4 h ST. (For interpretation of the references to color in this figure legend, the reader is referred to the web version of this article.)

remains practically unaffected (Fig. 2 and Fig. 3). Furthermore, a slight spheroidisation of eutectic and primary Si particles could be observed (see Fig. 1 and Fig. 2(c-d)), as expected during solution treatment of cast Al-Si alloys (e.g. [9,34]). Si spheroidisation is more pronounced in the case of binary near eutectic Al-Si alloys [12] and it decreases as the volume fraction of aluminides increases to form a hybrid 3D network of Si and aluminides [3,12]. The effect of solution heat treatment on these rigid 3D networks has been extensively reported, e.g. [1,3,5,33,35]. They are, from a topological point of view, fairly stable during solution treatment and only slight global changes in volume fraction, interconnectivity and morphology can be detected for alloys with near eutectic composition and additions of Cu and Ni [3,13] as in the case of the AlSi12Cu4Ni2 studied in this work.

Fig. 12 shows $V_f$, $I$, and Euler number for the aluminides in 0 h and 4 h ST conditions in a volume of 267 × 242 × 645 µm$^3$. While the aluminides are completely interconnected over the whole investigated volume, Si particles are present with an average size of 10–15 µm. A

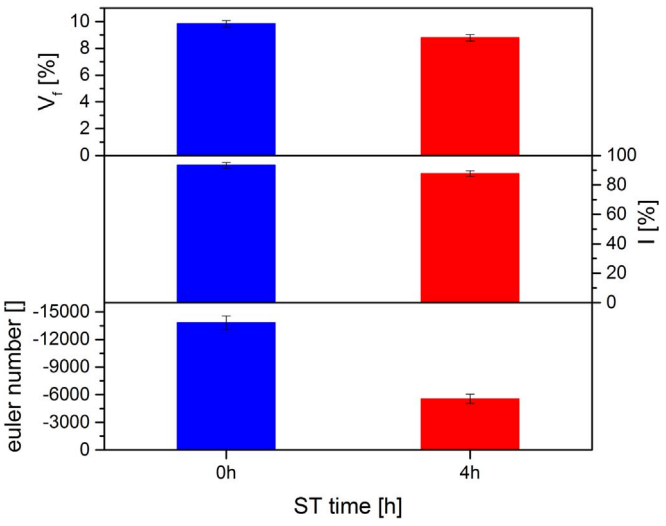


**Fig. 12.** Volume Fraction (Vf), Interconnectivity (I) and Euler number of aluminides for the 0 h and 4 h ST conditions.

decrease in volume fraction of aluminides of ~ 1 vol% (from 9.8 ± 0.25 vol% to 8.8 ± 0.23 vol%) and in interconnectivity of ~ 6% (from 93 ± 1.93% to 88 ± 1.86%) can be observed, while the Euler number, which describes the changes in local connectivity of the 3D network, evolves from −13824 to −5553 during ST (see Fig. 12). The latter indicates a loss of connecting branches within the network and can be attributed to the partial dissolution and morphological changes of $Al_2Cu$ (Fig. 3). A similar trend can be expected for the eutectic Si owing to the slight spheroidisation observed after 4 h ST (Fig. 2c–d). The effect of the highly interconnected 3D network of Si and aluminides as well as of the changes observed during ST on the damage of the alloy during tensile deformation is discussed in the following paragraphs.

The stress-strain curves obtained during the tensile tests (Fig. 5(a)) show a rather brittle behaviour in both the 0 h and 4 h ST conditions, with the latter displaying a strain hardening behaviour that results in a higher ductility than the alloy without solution treatment. The sXCT results show that damage starts preferably in areas with clusters of primary Si particles, where cracks perpendicular to the load direction accumulate. This could be a result of local stresses originating from developed micro-cracks through neighbouring Si particles. In general, rather than going through the comparatively soft Al-matrix, closely packed rigid particles facilitate the propagation of damage [36]. The influence of eutectic and primary Si on the damage behaviour of cast Al-Si alloys has been frequently reported [6,9,34,37–39]. Gangulee et. al. investigated theoretically and experimentally the fracture of Si particles in Al-Si alloys with Si concentrations between 2.8 and 13.2 wt % and reported that fracture generally appears in three stages: first, cracks initiate at Si particles, followed by propagation of cracks throughout interdendritic regions and finally, fracture of the Al-matrix [39]. Furthermore, the morphology of Si particles was found to play a significant role during tensile deformation. Fracture in unmodified, near eutectic A413.1 automotive alloys during RT tensile deformation preferentially occurs at brittle acicular Si particles rather than spherical ones [9,40].

No cracks originating from processing porosity or oxide inclusions were detected in the studied conditions. Previous investigations of Al-Si alloys under fatigue conditions reported that casting pores play a minor role as crack initiator for Si > 6–7 wt%, while alloys with higher Si contents show crack initiation preferably at Si and (Cu, Ni)-rich

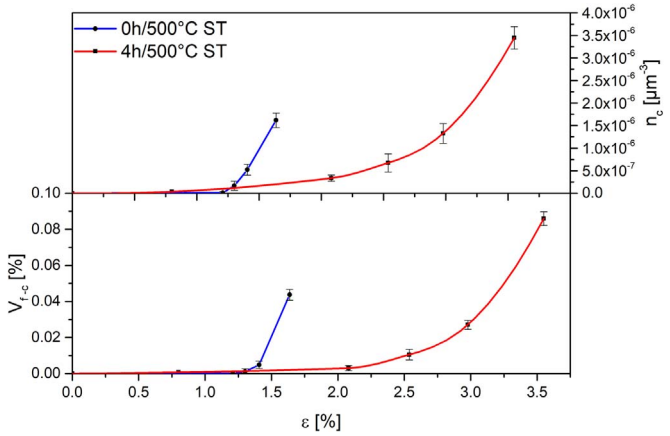


**Fig. 13.** Evolution of volume fraction (Vf (cracks)) and number density (n(cracks)) of microcracks during tensile deformation.

intermetallic phases [41].

Fig. 13 shows the evolution of crack number density, $n_c$, and crack volume fraction, $V_{f\text{-}c}$, during tensile deformation. The accumulation of damage in the 0 h ST condition accelerates already at $\varepsilon \sim 1\%$, as reflected by the increase of both $n_c$ and $V_{f\text{-}c}$ until fracture of the sample. On the other hand, the 4 h ST condition can accommodate more plastic deformation until acceleration in the process of damage is observed at $\varepsilon > 2.1\%$. $n_c$ and $V_{f\text{-}c}$ at fracture in the 4 h ST condition are a factor two higher than for 0 h ST, indicating that the alloy is able to resist twice as much damage before failure.

The difference in strength and damage accumulation to failure can be influenced by the strength of the α-Al matrix (e.g. [5,6,38]). However, while a drop in HB 1/10 hardness was measured for the alloy after 4 h ST, the hardness of the α-Al matrix determined by nano-hardness remains constant after the applied heat treatment (see Table 2). At constant grain size, the hardness of the α-Al matrix only depends on its precipitation condition and solid solution state, while the Brinell-hardness covers as well the effect of the other phases, i.e. interconnectivity and volume fraction of rigid phases [6,8]. This drop in Brinell-hardness during ST as a result of Si spheroidisation as well as morphological changes and dissolution of aluminides was also reported in literature [e.g. 3,10,11,13]. It can therefore be inferred that the differences observed in strength, ductility and damage accumulation between the 0 h and 4 h ST conditions are not a result of any changes in strength of the α-Al matrix since this remains constant after 4 h ST and the subsequent overaging (see Table 2). We propose that the loss of local connectedness of the aluminides (Fig. 8 and Fig. 12) and the slight spheroidisation of eutectic (and primary) Si (Fig. 2) provoke a loss of load carrying capability of the 3D network of Si and aluminides. This leads to a decrease of strength and an increase of ductility of the alloy in 4 h ST condition. This is in agreement with the theoretical work by A. Kruglova et. al. [29] where an increase in strength of an AlSi7 alloy could be correlated to a more negative Euler number of the 3D network formed by eutectic Si, i.e. higher connectedness of the load bearing phase.

Fig. 14 presents a schematic illustration of the different damage accumulation behaviours between the 0 h ST and 4 h ST conditions. In the 0 h ST condition the material is formed by a highly interconnected network of rigid phases with a high *connectedness* embedded in the α-Al matrix (see Fig. 14(a); light blue: prim. Si, dark blue: eutectic Si, yellow: aluminides, grey: matrix). In an early stage of deformation only a few cracks are formed through primary Si particles. As deformation proceeds, damage accumulates in the form of further cracks at clusters of primary Si particles. Finally, sudden failure occurs with the main crack propagating through the connected rigid phases (Si and aluminides) and pre-existing micro-cracks. In comparison, the 4 h ST condition shows less connecting branches within the highly interconnected network of rigid phases (Fig. 14(b)), i.e. less *connectedness*. Damage initiation occurs at a later deformation stage since the matrix is able to accommodate part of the plastic strain owing to the lower rigidity of the interconnected network. Therefore, the alloy in this condition is able to sustain more damage, which, similarly to the 0 h ST condition, accumulates as cracks in clusters of Si particles. Failure occurs by

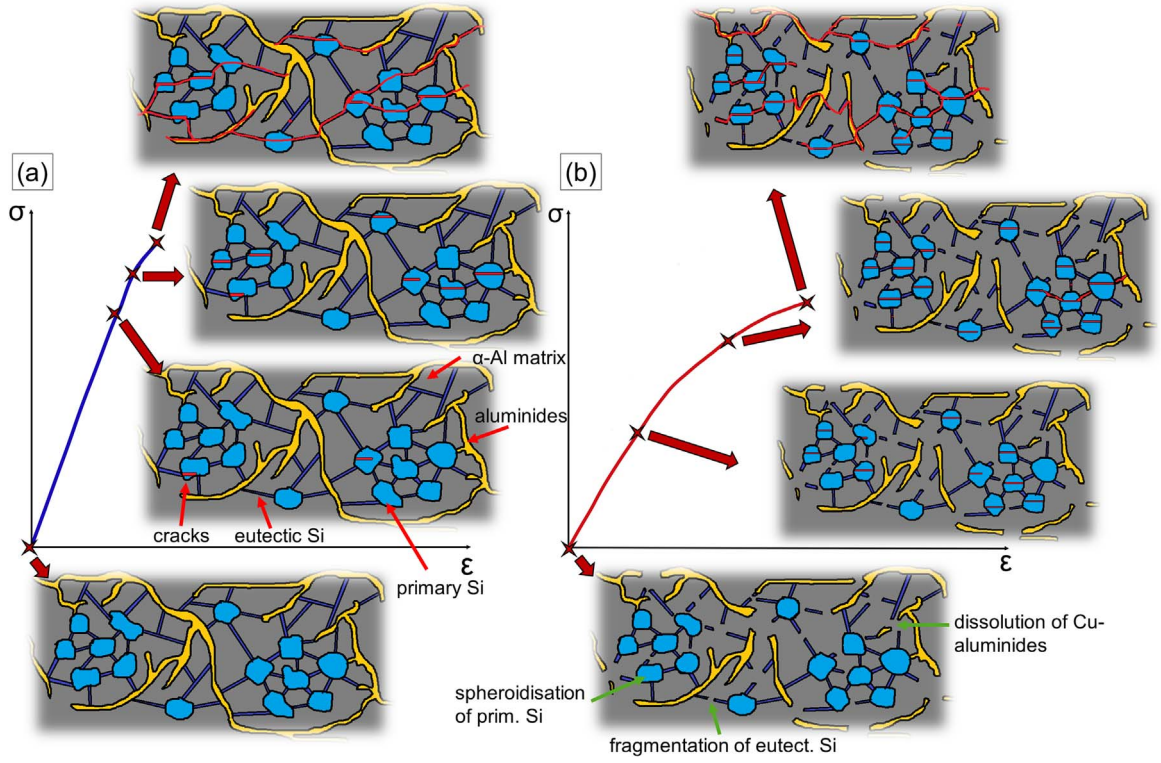


**Fig. 14.** Schematic illustration of the damage behaviour of the AlSi12Cu4Ni2 alloy (a) 0 h ST and (b) 4 h ST. The load direction is vertical.

coalescence of neighbouring micro-cracks, but the lower amount of connecting branches within the rigid networks implies that the main crack has less paths for rapid propagation and, thus, final fracture occurs at higher strain than in the 0 h ST condition.

## 5. Conclusions

The microstructural evolution as well as the damage mechanisms and damage evolution during tensile deformation were studied as a function of solution heat treatment for a cast AlSi12Cu4Ni2 piston alloy by conventional metallography combined with synchrotron tomography. The following conclusions are drawn:

- 4 h of solution treatment at 500 °C results in partial dissolution and morphological transformation of the $Al_2Cu$ phase from blocky into sponge-like structures. Also, slight spheroidisation of eutectic and primary Si was observed. These changes result in a loss of connecting branches, i.e. loss of connectedness, within the hybrid rigid network formed by Si and intermetallics usually found in this type of alloys, as reflected quantitatively by the evolution of the Euler number of the intermetallics network. The global connectivity, *I*, of the rigid networks formed by Si and the intermetallic compounds remains practically unaffected by the solution treatment.
- The alloy in both conditions shows that damage during tensile deformation begins in form of cracks preferably through primary Si particles and debonding at the interface between Si particles and α-Al. These cracks are oriented perpendicular to the load direction and tend to accumulate at clusters of primary Si particles.
- Final failure of the alloy in both conditions consists of coalescence of these cracks through the Si-intermetallics 3D networks. However, the loss in connectedness within these networks caused by the solution treatment allows the solution treated alloy to accommodate more damage and plastic strain inducing an increase of ductility compared to the 0 h ST condition.

## Acknowledgements

This work is part of the “K-Project for Non-Destructive Testing and Tomography Plus" supported by the COMET-Program of the Austrian Research Promotion Agency (FFG) as well as the Provinces of Upper Austria (LOÖ) and Styria, Grant No. 843540. The ESRF and DESY are acknowledged for the provision of synchrotron facilities at the beamlines ID19 and P05, respectively.

K. Bugelnig would like to acknowledge P. Wiehoff for support during segmentation of the tomography data.

## References

[1] The European Parliament and the Council of the European Union, Directive 2000/53/EC of the European Parliament and of the Council of 18 September 2000 on End-of-Life Vehicles, pp. 34–42, 2000.
[2] F.S. Silvia, Fatigue on engine pistons – a compendium of case studies, Eng. Fail. Anal. 13 (2006) 480–492.
[3] Z. Asghar, G. Requena, E. Boller, 3D rigid multiphase networks providing high-temperature strength to cast AlSi10Cu5Ni1-2 piston alloys, Acta Mater. 59 (2011) 6420–6432.
[4] D. Tolnai, G. Requena, P. Cloetens, J. Lendvai, H.P. Degischer, Effect of solution treatment on the internal architecture and compressive strength of an AlMg4,7Si alloy, Mater. Sci. Eng. A 585 (2013) 480–487.
[5] G. Requena, G. Garcés, Z. Asghar, E. Marks, P. Staron, P. Cloetens, The effect of connectivity of rigid phases on strength of Al-Si alloys, Adv. Eng. Mater. 13 (2011) 674–684.
[6] M. Schöbel, G. Baumgartner, S. Gerth, J. Bernardi, M. Hofmann, Microstresses and crack formation in AlSi7MgCu and AlSi17Cu4 alloys for engine components, Acta Mater. 81 (2014) 401–408.
[7] R. Fernández Gutiérrez, F. Sket, E. Maire, F. Wilde, E. Boller, G. Requena, Effect of solution treatment on microstructure and damage accumulation in cast Al-Cu alloys, J. Alloy. Compd. 697 (2017) 341–352.
[8] G.C. Requena, P. Degischer, E.D. Marks, E. Boller, Microtomographic study of the evolution of microstructure during creep of an AlSiCuMgNi alloy reinforced with Al2O3 short fibres, Mater. Sci. Eng. A 487 (2008) 99–107.
[9] M.A. Moustafa, F.H. Samuel, H.W. Doty, Effect of solution heat treatment and additives on the microstructure of Al-Si (A413.1) automotive alloys, J. Mater. Sci. 38 (2003) 4507–4522.
[10] A.M.A. Mohamed, F.H. Samuel, A Review on the Heat Treatment of Al-Si-Cu/Mg Casting Alloys, Intech, 2012, pp. 56–72.
[11] P.Y. Zhu, Q.Y. Liu, T.X. Hou, Spheroidization of eutectic silicon in aluminum-silicon alloys, AFS Trans. 93 (1985) 609–614.
[12] Z. Asghar, G. Requena, H.P. Degischer, P. Cloetens, Three-dimensional study of Ni aluminides in an AlSi12 alloy by means of light optical and synchrotron micro-tomography, Acta Mater. 57 (2009) 4125–4132.
[13] R. Koos, Correlation between 3D microstructure and thermo-mechanical behavior of near eutectic piston alloys, R. Koos, Correlation between 3D microstructure and thermo-mechanical behavior of near eutectic piston alloys, Ph.D. Thesis, TU Vienna, November, 2014., TU Vienna, November, 2014.
[14] Z. Asghar, G. Requena, G.H. Zahid, Rafi-ud-din, Effect of thermally stable Cu- and Mg-rich aluminides on the high temperature strength of an AlSi12CuMgNi alloy, Mater. Charact. 88 (X) (2017) 80–85.
[15] Z. Asghar, G. Requena, F. Kubel, The role of Ni and Fe aluminides on the elevated temperature strength of an AlSi12 alloy, Mater. Sci. Eng. A 527 (21–22) (2010) 5691–5698.
[16] Z. Asghar, G. Requena, Three dimensional post-mortem study of damage after compression of cast Al-Si alloys, Mater. Sci. Eng. A 591 (2014) 136–143.
[17] Z. Asghar, G. Requena, H.P. Degischer, E. Boller, Influence of Internal Architectures of Cast AlSi10Cu5Ni1-2 on High Temperature Strength, in: Proceedings of the 12th International Conference on Aluminium Alloys, Yokohama, Japan pp. 1285–1290, 2010.
[18] A. Tireira, G. Requena, S. Sao Jao, A. Borbely, H. Klocker, Rupture of intermetallic networks and strain localization in cast AlSi12Ni alloy: 2D and 3D characterization, Acta Mater. 112 (2016) 162–170.
[19] L. Babout, W. Ludwig, E. Maire, J.Y. Buffiere, J.Y. Buffi, Damage assessment in metallic structural materials using high resolution synchrotron X-ray tomography, Nucl. Instrum. Methods Phys. Res. Sect. B Beam Interact. Mater. At. 200 (2003) 303–307.
[20] J.Y. Buffière, H. Proudhon, E. Ferrie, W. Ludwig, E. Maire, P. Cloetens, Three dimensional imaging of damage in structural materials using high resolution micro-tomography, Nucl. Instrum. Methods Phys. Res. Sect. B Beam Interact. Mater. At. 238 (1–4) (2005) 75–82.
[21] E. Maire, S. Zhou, J. Adrien, M. Dimichiel, Damage quantification in aluminium alloys using *in situ* tensile tests in X-ray tomography, Eng. Fract. Mech. 78 (15) (2011) 2679–2690.
[22] J.Y. Buffière, E. Maire, P. Cloetens, G. Lormand, R. Fougères, Characterization of internal damage in a MMCp using X-ray synchrotron phase contrast micro-tomography, Acta Mater. 47 (5) (1999) 1613–1625.
[23] J.J. Gammage, D.S. Wilkinson *, J.D. Embury, E. Maire, Damage studies in heterogeneous aluminium alloys using X-ray tomography, Philos. Mag. 85 (26–27) (2005) 3191–3206.
[24] 〈http://www.esrf.eu/home/UsersAndScience/Experiments/StructMaterials/ID19.html 〉.
[25] F. Wilde, M. Ogurreck, I. Greving1, J.U. Hammel, F. Beckmann, A. Hipp, L. Lottermoser, I. Khokhriakov, P. Lytaev, T. Dose, H. Burmester, M. Müller, A. Schreyer, Micro-CT at the imaging beamline P05 at PETRA III, in: Proceedings of the AIP Conference, 1741, p. 030035, 2016.
[26] J. Schindelin, I. Arganda-Carreras, E. Frise, et al., Fiji: an open-source platform for biological-image analysis, Nat. Methods 9 (7) (2012) 676–682 (PMID 22743772).
[27] N. Toussaint, J.-.C. Souplet, P. Fillard, MedINRIA: Medical Image Navigation and Research Tool by INRIA. in: Proceedings of MICCAI '07 Workshop on Interaction in Medical Image Analysis and Visualization. Brisbane Australia, 2007.
[28] D.B. Aydogan, J. Hyttinen, Characterization of microstructures using contour tree connectivity for fluid flow analysis, R. Soc. Interface 11 (2014).
[29] A. Kruglova, M. Engstler, G. Gaiselmann, O. Stenzel, V. Schmidt, M. Roland, S. Diebels, F. Mücklich, 3D connectivity of eutectic Si as key property defining strength of Al-Si alloys, Comput. Mater. Sci. 120 (2016) 90–107.
[30] J. Toriwaki, T. Yonekura, Euler number and connectivity indexes of a three dimensional digital picture, Forma 17 (3) (2003) 183–209.
[31] N.A. Belov, D.G. Eskin, N.N. Avxentieva, Constituent phase diagrams of the Al-Cu-Fe-Mg-Ni-Si system and their application to the analysis of aluminium piston alloys, Acta Mater. 53 (17) (2005) 4709–4722.
[32] E. Tillová, M. Chalupová, L. Hurtalová, M. Bonek, L.A. Dobrzański, Structural analysis of heat treated automotive cast alloy, J. Achiev. Mater. Manuf. Eng. 47 (1) (2011) 19–25.
[33] F. Lasagni, A. Lasagni, E. Marks, C. Holzapfel, F. Mücklich, H.P. Degischer, Three-dimensional characterization of ‘as-cast’ and solution-treated AlSi12(Sr) alloys by high-resolution FIB tomography, Acta Mater. 55 (11) (2007) 3875–3882.
[34] Y. Han, A.M. Samuel, H.W. Doty, S. Valtierra, F.H. Samuel, Optimizing the tensile properties of Al-Si-Cu-Mg 319-type alloys: role of solution heat treatment, Mater. Des. 58 (2014) 426–438.
[35] M. Lebyodkin, A. Deschamps, Y. Bréchet, Influence of second phase morphology and topology on mechanical and fracture properties of Al-Si alloys, Mater. Sci. Eng. A 234–236 (1997) 481–484.
[36] G. Zhang, J. Zhang, B. Li, W. Cai, Characterization of tensile fracture in heavily alloyed Al-Si piston alloy, Prog. Nat. Sci.: Mater. Int. 21 (2011) 380–385.
[37] M.A. Moustafa, F.H. Samuel, H.W. Doty, Effect of solution heat treatment and additives on the hardness, tensile properties and fracture behavior of Al-Si (A413.1) automotive alloys, J. Mater. Sci. 38 (2003) 4523–4534.
[38] T.O. Mbuya, P.A.S. Reed, Micromechanisms of short fatigue crack growth in an Al-Si piston alloy, Mater. Sci. Eng. A 612 (2014) 302–309.
[39] A. Gangulee, J. Gurland, On the fracture of silicon particles in Al-Si alloys, Trans. Metall. Soc. AIME 239 (2) (1967) 269–272.
[40] J. Feng, Su, X. Nie, V. Stoilov, Characterization of fracture and debonding of Si particles in AlSi alloys, Mater. Sci. Eng. A 527 (2010) 7168–7175.
[41] T.O. Mbuya, I. Sinclair, A.J. Moffat, P.A.S. Reed, Micromechanisms of fatigue crack growth in cast aluminum piston alloys, Int. J. Fatigue 42 (2012) 227–237.